Available online at www.eccomasproceedia.org
Eccomas Proceedia COMPDYN (2023) 2983-2995

ECCOMAS
Proceedia

COMPDYN 2023
9th ECCOMAS Thematic Conference on
Computational Methods in Structural Dynamics and Earthquake Engineering
M. Papadrakakis, M. Fragiadakis (eds.)
Athens, Greece, 12-14 June 2023

EFFECT OF THE LENGTH OF SEISMIC METASURFACES ON VIBRATION MITIGATION PERFORMANCE

David Carneiro, Pieter Reumers, Geert Lombaert, and Geert Degrande

KU Leuven, Department of Civil Engineering, Structural Mechanics Section
Kasteelpark Arenberg 40 box 2448, B-3001 Leuven, Belgium
e-mail: david.carneiro@kuleuven.be

Abstract. *This paper investigates the effect of the length of 2D seismic metasurfaces composed of an array of resonators on vibration mitigation performance. This is accomplished by means of computations using 3D and periodic finite element - boundary element (FE-BE) models. Whereas the 3D model considers a finite number of resonators on layered soils, the periodic approach assumes an infinite number of equally spaced resonators in the longitudinal direction. Behind longer metasurfaces, larger vibration reduction is found in a perpendicular direction from the source. The vibration mitigation performance of the metasurfaces reduces with distance from the source. The number of resonators also affects the frequency at which the metasurface has the best performance. The advantage of the periodic model is that only a line of resonators needs to be modeled resulting in a reduction in computational requirements. The computation time, however, depends on the number of terms in the Floquet transform, which is affected by the spacing between the resonators and the dynamic soil characteristics. Larger spacing increases the maximum distance between the periodic sources. Waves traveling on highly damped soils vanish at shorter distances. This enables a reduction of the number of terms in the Floquet transform and the use of coarser wavenumber samplings while still accurately predicting the response of metasurfaces.*

Keywords: Periodic seismic metasurfaces, dynamic soil-structure interaction, boundary element method.

ISSN:2623-3347
Peer-review under responsibility of the organizing committee of COMPDYN 2023.
doi: 10.7712/120123.10616.20809

1 Introduction

Seismic metamaterials have been widely investigated as a vibration mitigation measure over the past years. These are artificially engineered materials consisting of an arrangement of elementary cells exhibiting non-conventional dispersion properties that are usually not found in natural soils [1]. Non-resonant metamaterials induce Bragg scattering as a result of periodic arrangements of the same order of the surface wavelengths. Locally resonant metamaterials do not rely on structural periodicity, allowing their dimensions and spacings to be lower than the surface wavelengths [2].

Locally resonant seismic metasurfaces consisting of an array of resonators are employed in this paper. Their vibration mitigation performance depends on the soil properties, the number and arrangement of the resonators and their dynamic properties [3]. We focus on the effect of the number of resonators in the longitudinal direction for a fixed number of resonators in the perpendicular direction.

The band gap created by an array of resonators on a homogeneous halfspace under an incoming wave field from fixed sources can be predicted using numerical models [4]. Resonators with identical resonance frequency placed on top of a homogeneous soil induce narrow band gaps [5, 6]. This can be broadened over a wider frequency band using graded metamaterials [7]. 2D models considering uniform geometry in the longitudinal direction are frequently employed. In reality, metabarriers have finite dimensions in both directions. Therefore, their length in the longitudinal direction plays a crucial role, requiring further investigation.

The large computational cost to model a finite metabarrier interacting with soil is still a concern, in particular for very long and wide metabarriers in a broad frequency range. Numerical analyses are usually made with a finite element (FE) model coupled with absorbing boundary conditions such as perfectly matched layers (PML), as commonly available in commercial softwares [6, 8, 9]. This results in straightforward discretization and computation for both metasurfaces and embedded metabarriers. Extended 3D FE-PML meshes may become computationally very demanding, however.

Alternatively, coupled FE-BE formulations are developed to analyze the performance of seismic metabarriers [4]. As fundamental solutions of a layered halfspace can be employed, the boundary element (BE) mesh remains limited to the soil-structure interfaces. The drawback of this method is that fully populated matrices lead to high memory and CPU requirements, hindering the applicability of the BE method for a large number of resonators. In the case of metasurfaces with a periodic layout, an alternative is to model a slice of soil containing resonators using a periodic FE-BE model [10], resulting in a reduction of the computational requirements.

This paper investigates the effect of the number of resonators in the longitudinal direction on the vibration mitigation performance of metasurfaces. 3D and periodic FE-BE models are used to solve this problem. The periodic approach assumes a finite number of resonators in one direction and an infinite number of equally spaced resonators in the other direction. The corresponding formulations are developed for multiple resonators on top of layered soils. The excitation is a vertical harmonic point load applied on the surface of the soil. The computational performance of a periodic FE-BE model is compared with the 3D FE-BE model. We gradually increase the length of the metasurface in the longitudinal direction using a 3D FE-BE model, approaching the case of an infinitely long periodic metasurface. We assess the vibration mitigation performance of different configurations by computing the wave field on the surface of the soil and the corresponding insertion loss at selected receiver points behind the metasurfaces.

Memory requirements for computing boundary element matrices and CPU time are given.

The outline of the paper is as follows. Section 2 presents a 3D and periodic FE-BE formulation for a metasurface on layered soils. The vibration mitigation performance of seismic metasurfaces on a homogeneous soil and computational efficiency of the FE-BE models are described in section 3. Section 4 concludes the paper.

2 Seismic metasurface on a layered soil

2.1 Problem outline

Figure 1a depicts a finite metasurface comprising an array of N resonators on top of a layered soil represented by the unbounded domain $\Omega_{\mathrm{s}}^{\mathrm{e}}$. The metasurface is placed at a perpendicular distance D from the origin of the coordinate system. The layout is characterized by a rectangular grid of N_x by N_y resonators with lattice constants a_x and a_y in the x- and y-direction, respectively. The interface between a resonator k and the soil is defined as Σ_k. The soil-structure interface for N resonators is denoted as $\Sigma = \bigcup_{k=1}^{N} \Sigma_k$.

In cases where the array of resonators has a periodic arrangement, N_x resonators in the x-direction and an infinite number of equally spaced resonators in the y-direction ($N_y = \infty$) are considered. The domain can then be restricted to a reference cell $\tilde{\Omega}_{\mathrm{s}}^{\mathrm{e}}$ with period $L = a_y$ in the longitudinal direction $\mathbf{e}_y$ (figure 1b).

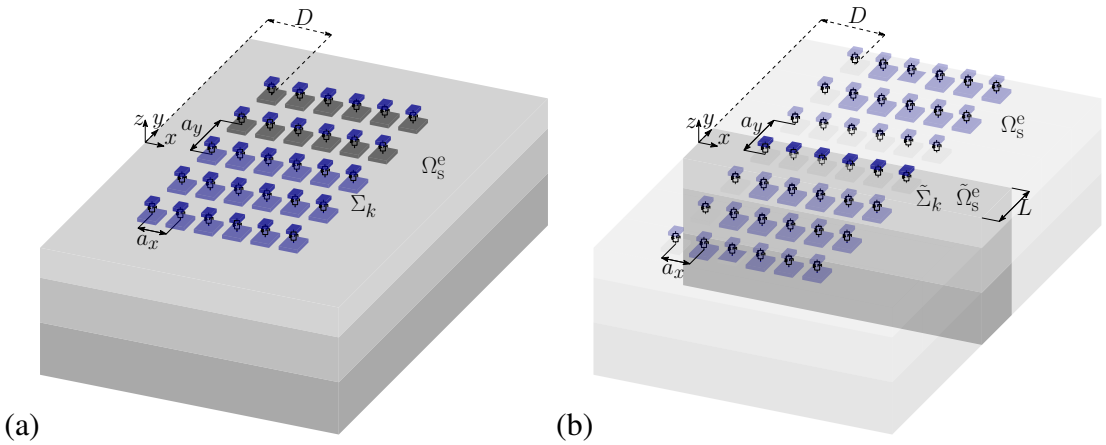

(a) (b)

Figure 1: (a) Finite and (b) periodic array of resonators.

2.2 3D FE-BE model

2.2.1 Displacement and traction fields

The displacement of a resonator k on top of the layered halfspace is denoted as $\hat{\mathbf{u}}_{\mathrm{r}k}(\mathbf{x}, \omega)$. A hat on a variable denotes its representation in the spatial-frequency domain. Continuity conditions and equilibrium of tractions are imposed on the soil-resonator interface Σ_k:

$$\hat{\mathbf{u}}_{\mathrm{r}k} - \hat{\mathbf{u}}_{\mathrm{s}} = \mathbf{0} \quad \text{on} \quad \Sigma_k \tag{1}$$

$$\hat{\mathbf{t}}_{\mathrm{r}}(\hat{\mathbf{u}}_{\mathrm{r}k}) + \hat{\mathbf{t}}_{\mathrm{s}}(\hat{\mathbf{u}}_{\mathrm{s}}) = \mathbf{0} \quad \text{on} \quad \Sigma_k, \tag{2}$$

where $\hat{\mathbf{u}}_{\mathrm{s}}(\mathbf{x}, \omega)$ is the soil displacement vector and $\hat{\mathbf{t}}_{\mathrm{r}}(\hat{\mathbf{u}}_{\mathrm{r}k})(\mathbf{x}, \omega)$ is the traction vector due to the displacement $\hat{\mathbf{u}}_{\mathrm{r}k}$.

Assuming that the resonators are subjected to an incident wave field, the soil displacement $\hat{\mathbf{u}}_{\mathrm{s}}(\mathbf{x},\omega)$ is decomposed into the incident wave field $\hat{\mathbf{u}}_{\mathrm{inc}}(\mathbf{x},\omega)$, the locally diffracted wave field $\hat{\mathbf{u}}_{\mathrm{d0}}(\mathbf{x},\omega)$ and the wave field $\hat{\mathbf{u}}_{\mathrm{sc}}(\mathbf{x},\omega)$ scattered by the displacements $\hat{\mathbf{u}}_{\mathrm{r}k}(\mathbf{x},\omega)$ of all resonators k ($k=1,\ldots,N$) such that [11]:

$$\hat{\mathbf{u}}_{\mathrm{s}} = \hat{\mathbf{u}}_{\mathrm{inc}} + \hat{\mathbf{u}}_{\mathrm{d0}} + \sum_{k=1}^{N} \hat{\mathbf{u}}_{\mathrm{sc}}(\hat{\mathbf{u}}_{\mathrm{r}k}). \tag{3}$$

The incident wave field $\hat{\mathbf{u}}_{\mathrm{inc}}$ is computed with a source model. The locally diffracted wave field $\hat{\mathbf{u}}_{\mathrm{d0}}(\mathbf{x},\omega)$ is an elastodynamic field that obeys Sommerfeld's radiation condition. This is defined so that the combined wave field $\hat{\mathbf{u}}_{\mathrm{inc}}(\mathbf{x},\omega) + \hat{\mathbf{u}}_{\mathrm{d0}}(\mathbf{x},\omega)$ vanishes on the soil-structure interface Σ.

2.2.2 Soil-structure interaction problem

The dynamic equilibrium for a single structure j ($j=1,\ldots,N$) can be expressed in a weak variational form. A virtual displacement field $\hat{\mathbf{v}}_{\mathrm{r}j}(\mathbf{x},\omega)$ is imposed on the structure j in order to construct the virtual work expression, which is given by [12]:

$$\int_{\Omega_{\mathrm{r}j}} \hat{\boldsymbol{\epsilon}}_{\mathrm{r}}(\hat{\mathbf{v}}_{\mathrm{r}j}) : \hat{\boldsymbol{\sigma}}_{\mathrm{r}}(\hat{\mathbf{u}}_{\mathrm{r}j})\,\mathrm{d}\Omega - \omega^2 \int_{\Omega_{\mathrm{r}j}} \hat{\mathbf{v}}_{\mathrm{r}j}\cdot\rho_{\mathrm{r}j}\hat{\mathbf{u}}_{\mathrm{r}j}\,\mathrm{d}\Omega = \int_{\Sigma_j} \hat{\mathbf{v}}_{\mathrm{r}j}\cdot\hat{\mathbf{t}}_{\mathrm{r}}(\hat{\mathbf{u}}_{\mathrm{r}j})\,\mathrm{d}\Gamma, \tag{4}$$

where $\hat{\boldsymbol{\epsilon}}_{\mathrm{r}}(\hat{\mathbf{v}}_{\mathrm{r}j})(\mathbf{x},\omega)$ is the virtual strain tensor, $\hat{\boldsymbol{\sigma}}_{\mathrm{r}}(\hat{\mathbf{u}}_{\mathrm{r}j}))(\mathbf{x},\omega)$ is the Cauchy stress tensor due to displacements $\hat{\mathbf{u}}_{\mathrm{r}j}(\mathbf{x},\omega)$, and $\rho_{\mathrm{r}j}$ is the density of the structure. Introducing equations (2) and (3) into equation (4) yields:

$$\begin{aligned}\int_{\Omega_{\mathrm{r}j}} \hat{\boldsymbol{\epsilon}}_{\mathrm{r}}(\hat{\mathbf{v}}_{\mathrm{r}j}) : \hat{\boldsymbol{\sigma}}_{\mathrm{r}}(\hat{\mathbf{u}}_{\mathrm{r}j})\,\mathrm{d}\Omega - \omega^2 \int_{\Omega_{\mathrm{r}j}} \hat{\mathbf{v}}_{\mathrm{r}j}\cdot\rho_{\mathrm{r}j}\hat{\mathbf{u}}_{\mathrm{r}j}\,\mathrm{d}\Omega + \sum_{k=1}^{N}\int_{\Sigma_j} \hat{\mathbf{v}}_{\mathrm{r}j}\cdot\hat{\mathbf{t}}_{\mathrm{s}}(\hat{\mathbf{u}}_{\mathrm{sc}}(\hat{\mathbf{u}}_{\mathrm{r}k}))\,\mathrm{d}\Gamma \\ = -\int_{\Sigma_j} \hat{\mathbf{v}}_{\mathrm{r}j}\cdot\hat{\mathbf{t}}_{\mathrm{s}}(\hat{\mathbf{u}}_{\mathrm{inc}} + \hat{\mathbf{u}}_{\mathrm{d0}})\,\mathrm{d}\Gamma.\end{aligned} \tag{5}$$

This problem is solved by means of a coupled FE-BE model. The resonator is modeled with finite elements whereas boundary elements are used to discretize the unbounded soil on the interfaces Σ_k. The structural displacement vector for resonator j is discretized as:

$$\hat{\mathbf{u}}_{\mathrm{r}j} \simeq \mathbf{N}_{\mathrm{r}j}\underline{\hat{\mathbf{u}}}_{\mathrm{r}j}, \tag{6}$$

where $\mathbf{N}_{\mathrm{r}j}$ is a matrix of global finite element shape functions for resonator j and $\underline{\hat{\mathbf{u}}}_{\mathrm{r}j}(\omega)$ is the vector with nodal degrees of freedom. In a Galerkin approach, this approximation is also used for the virtual displacement field $\hat{\mathbf{v}}_{\mathrm{r}}(\mathbf{x},\omega)$. Equation (5) then yields:

$$\left[\mathbf{K}_j - \omega^2\mathbf{M}_j\right]\underline{\hat{\mathbf{u}}}_{\mathrm{r}j} + \sum_{k=1}^{N}\hat{\mathbf{K}}^{\mathrm{s}}_{jk}\underline{\hat{\mathbf{u}}}_{\mathrm{r}k} = \underline{\hat{\mathbf{f}}}^{\mathrm{s}}_{j}, \tag{7}$$

where $\mathbf{K}_j$ and $\mathbf{M}_j$ are the stiffness and mass matrices of the resonator j, respectively. The contribution of structural damping can be added to equation (7). In this work, proportional

damping is used where a damping ratio is defined for each mode of the structure. The summation in equation (7) accounts for through-soil coupling of resonator j with all resonators. The soil stiffness matrix $\hat{\mathbf{K}}^{\mathrm{s}}_{jk}(\omega)$ is given by:

$$\hat{\mathbf{K}}^{\mathrm{s}}_{jk} = \int_{\Sigma_j} \mathbf{N}^{\mathrm{T}}_{\mathrm{r}j} \hat{\mathbf{t}}_{\mathrm{s}}(\hat{\mathbf{u}}_{\mathrm{sc}}(\mathbf{N}_{\mathrm{r}k}))\,\mathrm{d}\Gamma. \tag{8}$$

The force vector $\hat{\underline{\mathbf{f}}}^{\mathrm{s}}_{j}(\omega)$ due to an incident wave field is equal to:

$$\hat{\underline{\mathbf{f}}}^{\mathrm{s}}_{j} = -\int_{\Sigma_j} \mathbf{N}^{\mathrm{T}}_{\mathrm{r}j} \hat{\mathbf{t}}_{\mathrm{s}}(\hat{\mathbf{u}}_{\mathrm{inc}} + \hat{\mathbf{u}}_{\mathrm{d0}})\,\mathrm{d}\Gamma. \tag{9}$$

The scattered wave field and the locally diffracted wave field are computed by means of the BE method, as the problem is formulated in terms of displacements on the interfaces Σ_k. When the resonator j is placed on the surface of the soil, $\hat{\mathbf{t}}_{\mathrm{s}}(\hat{\mathbf{u}}_{\mathrm{inc}})(\omega) = \mathbf{0}$. The tractions $\hat{\mathbf{t}}_{\mathrm{s}k}(\omega)$ on the soil-resonator interfaces are calculated as:

$$\sum_{k=1}^{N} \left[\mathbf{I}_{jk} + \hat{\mathbf{T}}_{jk}\right] \hat{\underline{\mathbf{u}}}_{\mathrm{s}k} = \sum_{k=1}^{N} \hat{\mathbf{U}}_{jk} \hat{\underline{\mathbf{t}}}_{\mathrm{s}k}, \tag{10}$$

where $\mathbf{I}_{jk}$ is an identity matrix, $\hat{\mathbf{U}}_{jk}(\omega)$ and $\hat{\mathbf{T}}_{jk}(\omega)$ are fully populated asymmetric boundary element matrices which require the integration of Green's functions for a layered halfspace, and $\hat{\underline{\mathbf{u}}}_{\mathrm{s}k}(\omega)$ and $\hat{\underline{\mathbf{t}}}_{\mathrm{s}k}(\omega)$ are the displacements and tractions on the soil-structure interface Σ_k. For a BE mesh on the surface of the soil, $\hat{\mathbf{T}}_{jk}(\omega) = \mathbf{0}$.

2.2.3 Craig-Bampton substructuring method

It is convenient to decompose the structural displacement vector $\hat{\underline{\mathbf{u}}}_{\mathrm{r}j}(\omega)$ of resonator j into displacements of its foundation $\hat{\underline{\mathbf{u}}}_{\mathrm{r}_1 j}(\omega)$ and superstructure $\hat{\underline{\mathbf{u}}}_{\mathrm{r}_2 j}(\omega)$. Introducing this decomposition into equation (6) leads to:

$$\hat{\mathbf{u}}_{\mathrm{r}j} \simeq \begin{bmatrix} \mathbf{N}_{\mathrm{r}_1 j} & \mathbf{N}_{\mathrm{r}_2 j} \end{bmatrix} \begin{Bmatrix} \hat{\underline{\mathbf{u}}}_{\mathrm{r}_1 j} \\ \hat{\underline{\mathbf{u}}}_{\mathrm{r}_2 j} \end{Bmatrix}. \tag{11}$$

Using the decomposition (11), equation (7) becomes:

$$\begin{aligned} \left(\begin{bmatrix} \mathbf{K}_{\mathrm{r}_1\mathrm{r}_1 j} & \mathbf{K}_{\mathrm{r}_1\mathrm{r}_2 j} \\ \mathbf{K}_{\mathrm{r}_2\mathrm{r}_1 j} & \mathbf{K}_{\mathrm{r}_2\mathrm{r}_2 j} \end{bmatrix} - \omega^2 \begin{bmatrix} \mathbf{M}_{\mathrm{r}_1\mathrm{r}_1 j} & \mathbf{M}_{\mathrm{r}_1\mathrm{r}_2 j} \\ \mathbf{M}_{\mathrm{r}_2\mathrm{r}_1 j} & \mathbf{M}_{\mathrm{r}_2\mathrm{r}_2 j} \end{bmatrix} \right) \begin{Bmatrix} \hat{\underline{\mathbf{u}}}_{\mathrm{r}_1 j} \\ \hat{\underline{\mathbf{u}}}_{\mathrm{r}_2 j} \end{Bmatrix} \\ + \sum_{k=1}^{N} \begin{bmatrix} \hat{\mathbf{K}}^{\mathrm{s}}_{\mathrm{r}_1\mathrm{r}_1 jk} & \mathbf{0} \\ \mathbf{0} & \mathbf{0} \end{bmatrix} \begin{Bmatrix} \hat{\underline{\mathbf{u}}}_{\mathrm{r}_1 k} \\ \hat{\underline{\mathbf{u}}}_{\mathrm{r}_2 k} \end{Bmatrix} = \begin{Bmatrix} \hat{\underline{\mathbf{f}}}^{\mathrm{s}}_{\mathrm{r}_1 j} \\ \mathbf{0} \end{Bmatrix}. \end{aligned} \tag{12}$$

Since the resonator is composed of a superstructure coupled to a foundation interacting with the soil, it is advantageous to use a Craig-Bampton substructuring technique [13]. This reduces the problem size and avoids the recomputation of the BE matrices for the same dimensions and spacing of foundations whenever the superstructures change. Using the Craig-Bampton substructuring technique, the displacement vector $\hat{\mathbf{u}}_{\mathrm{r}j}$ of resonator j is written as:

$$\hat{\mathbf{u}}_{\mathrm{r}j} = \begin{bmatrix} \mathbf{N}_{\mathrm{r}_1 j} & \mathbf{N}_{\mathrm{r}_2 j} \end{bmatrix} \begin{bmatrix} \boldsymbol{\Phi}_{\mathrm{r}_1 j} & \mathbf{0} \\ \boldsymbol{\Phi}^{\mathrm{s}}_{\mathrm{r}_2 j} & \boldsymbol{\Phi}_{\mathrm{r}_2 j} \end{bmatrix} \begin{Bmatrix} \hat{\underline{\boldsymbol{\alpha}}}_{\mathrm{r}_1 j} \\ \hat{\underline{\boldsymbol{\alpha}}}_{\mathrm{r}_2 j} \end{Bmatrix} = \mathbf{N}_{\mathrm{r}j} \boldsymbol{\Phi}_{\mathrm{r}j} \hat{\underline{\boldsymbol{\alpha}}}_{\mathrm{r}j}, \tag{13}$$

where the vector $\underline{\hat{\boldsymbol{\alpha}}}_{\mathrm{r}j}(\omega)$ collects the modal coordinates. The modes $\boldsymbol{\Phi}_{\mathrm{r}_2 j}$ are the eigenmodes of the superstructure with clamped base. The modes $\boldsymbol{\Phi}_{\mathrm{r}_1 j}$ are the eigenmodes of the foundation without the superstructure. The modes $\boldsymbol{\Phi}^{\mathrm{s}}_{\mathrm{r}_2 j}$ are the quasi-static transmission of the foundation modes $\boldsymbol{\Phi}_{\mathrm{r}_1 j}$ into the superstructure:

$$\boldsymbol{\Phi}^{\mathrm{s}}_{\mathrm{r}_2 j} = -\mathbf{K}^{-1}_{\mathrm{r}_2\mathrm{r}_2 j}\mathbf{K}_{\mathrm{r}_2\mathrm{r}_1 j}\boldsymbol{\Phi}_{\mathrm{r}_1 j}, \tag{14}$$

where $\mathbf{K}_{\mathrm{r}_2\mathrm{r}_2 j}$ and $\mathbf{K}_{\mathrm{r}_2\mathrm{r}_1 j}$ are submatrices of the stiffness matrix of resonator j presented in equation (12). Introducing equation (13) in equation (5) and premultiplying with $\boldsymbol{\Phi}^{\mathrm{T}}_{\mathrm{r}j}$ gives:

$$\boldsymbol{\Phi}^{\mathrm{T}}_{\mathrm{r}j}\left[\mathbf{K}_j - \omega^2\mathbf{M}_j\right]\boldsymbol{\Phi}_{\mathrm{r}j}\underline{\hat{\boldsymbol{\alpha}}}_{\mathrm{r}j} + \sum_{k=1}^{N}\boldsymbol{\Phi}^{\mathrm{T}}_{\mathrm{r}j}\hat{\mathbf{K}}^{\mathrm{s}}_{jk}\boldsymbol{\Phi}_{\mathrm{r}k}\underline{\hat{\boldsymbol{\alpha}}}_{\mathrm{r}k} = \boldsymbol{\Phi}^{\mathrm{T}}_{\mathrm{r}j}\underline{\hat{\mathbf{f}}}^{\mathrm{s}}_{j}. \tag{15}$$

The modal soil stiffness matrix $\boldsymbol{\Phi}^{\mathrm{T}}_{\mathrm{r}_1 j}\hat{\mathbf{K}}^{\mathrm{s}}_{\mathrm{r}_1\mathrm{r}_1 jk}\boldsymbol{\Phi}_{\mathrm{r}_1 k}$ is given by:

$$\boldsymbol{\Phi}^{\mathrm{T}}_{\mathrm{r}_1 j}\hat{\mathbf{K}}^{\mathrm{s}}_{\mathrm{r}_1\mathrm{r}_1 jk}\boldsymbol{\Phi}_{\mathrm{r}_1 k} = \int_{\Sigma_j}\boldsymbol{\Phi}^{\mathrm{T}}_{\mathrm{r}_1 j}\mathbf{N}^{\mathrm{T}}_{\mathrm{r}_1 j}\hat{\mathbf{t}}_{\mathrm{s}}(\hat{\mathbf{u}}_{\mathrm{sc}}(\mathbf{N}_{\mathrm{r}_1 k}\boldsymbol{\Phi}_{\mathrm{r}_1 k}))\,\mathrm{d}\Gamma. \tag{16}$$

The modal soil tractions $\hat{\mathbf{t}}_{\mathrm{s}}(\hat{\mathbf{u}}_{\mathrm{sc}}(\mathbf{N}_{\mathrm{r}_1 k}\boldsymbol{\Phi}_{\mathrm{r}_1 k}))(\omega)$ are computed by means of equation (10) for each mode and integrated over the interface using equation (16).

Modifications of the superstructure do not affect the computation of the soil stiffness in equation (16) as it only depends on the foundation modes and the BE mesh.

2.3 Receiver points

Tractions $\underline{\hat{\mathbf{t}}}_{\mathrm{s}}(\omega)$ and displacements $\underline{\hat{\mathbf{u}}}_{\mathrm{s}}(\omega)$ on the interface Σ are computed according to the procedure described in [4]. The radiated wave field $\underline{\hat{\mathbf{u}}}^{\mathrm{r}}_{\mathrm{s}}(\mathbf{x},\omega)$ in the soil domain $\Omega^{\mathrm{e}}_{\mathrm{s}}$ is evaluated as:

$$\underline{\hat{\mathbf{u}}}^{\mathrm{r}}_{\mathrm{s}} = \hat{\mathbf{U}}_{\mathrm{p}}\underline{\hat{\mathbf{t}}}_{\mathrm{s}} - \hat{\mathbf{T}}_{\mathrm{p}}\underline{\hat{\mathbf{u}}}_{\mathrm{s}}, \tag{17}$$

where $\hat{\mathbf{U}}_{\mathrm{p}}(\mathbf{x},\omega)$ and $\hat{\mathbf{T}}_{\mathrm{p}}(\mathbf{x},\omega)$ are boundary element transfer matrices computed with the Green's functions of a layered halfspace.

2.4 Periodic FE-BE model

Although a substantial reduction in computation time and memory requirements can be achieved using the Craig-Bamption method, the computation of the modal soil stiffness matrices can still be very demanding for a large number of resonators N. Alternatively, a periodic FE-BE formulation is proposed in combination with a Craig-Bampton substructuring method [14].

The problem in figure 1a can be limited to a reference cell $\tilde{\Omega}^{\mathrm{e}}_{\mathrm{s}}$ (figure 1b) by application of Floquet's theorem. The position vector $\mathbf{x}$ in the problem domain $\Omega^{\mathrm{e}}_{\mathrm{s}}$ can be decomposed into $\mathbf{x} = \tilde{\mathbf{x}} + n_y L\mathbf{e}_y$, where $\tilde{\mathbf{x}}$ is the position vector in the reference cell $\tilde{\Omega}^{\mathrm{e}}_{\mathrm{s}}$ and n_y is the cell number. The Floquet transformation $\tilde{f}(\tilde{\mathbf{x}},\kappa_y)$ of a non-periodic function $f(\mathbf{x}) = f(\tilde{\mathbf{x}} + n_y L\mathbf{e}_y)$ defined on a 3D domain $\Omega^{\mathrm{e}}_{\mathrm{s}}$, that is periodic in the y-direction with period L, transforms the distance $n_y L$ between the n_yth cell and the reference cell $\tilde{\Omega}^{\mathrm{e}}_{\mathrm{s}}$ to the wavenumber $\kappa_y \in]-\pi/L, +\pi/L[$ and is defined as [10]:

$$\tilde{f}(\tilde{\mathbf{x}},\kappa_y) = \sum_{n_y=-\infty}^{\infty} f(\tilde{\mathbf{x}} + n_y L\mathbf{e}_y)\exp\left(+\mathrm{i}n_y L\kappa_y\right). \tag{18}$$

The complex function $\tilde{f}(\tilde{\mathbf{x}}, \kappa_y)$ is a periodic function of κ_y with a period $2\pi/L$ (or a periodic function of the first kind with respect to κ_y), as the following periodicity condition holds [10]:

$$\tilde{f}\left(\tilde{\mathbf{x}}, \kappa_y + \frac{2\pi}{L}\right) = \tilde{f}(\tilde{\mathbf{x}}, \kappa_y). \tag{19}$$

This complex function $\tilde{f}(\tilde{\mathbf{x}}, \kappa_y)$ is also periodic of the second kind with a period L in the y-direction, since the following condition holds for all $\tilde{\mathbf{x}}$ [10]:

$$\tilde{f}(\tilde{\mathbf{x}} + L\mathbf{e}_y, \kappa_y) = \exp\left(+\mathrm{i}\kappa_y L\right)\tilde{f}(\tilde{\mathbf{x}}, \kappa_y). \tag{20}$$

The function $f(\tilde{\mathbf{x}} + n_y L\mathbf{e}_y)$ can be reconstructed for any $\mathbf{x} = \tilde{\mathbf{x}} + n_y L\mathbf{e}_y$ using the inverse Floquet transform [10]:

$$f(\tilde{\mathbf{x}} + n_y L\mathbf{e}_y) = \frac{L}{2\pi}\int_{-\pi/L}^{\pi/L} \tilde{f}(\tilde{\mathbf{x}}, \kappa_y)\exp\left(-\mathrm{i}n_y L\kappa_y\right)\mathrm{d}\kappa_y \tag{21}$$

Using the Floquet transformation defined in equation (18), all the displacement and traction fields $\hat{\mathbf{u}}(\mathbf{x}, \omega)$ and $\hat{\mathbf{t}}(\mathbf{x}, \omega)$ in the domain $\Omega_{\mathrm{s}}^{\mathrm{e}}$ are transformed to the fields $\tilde{\mathbf{u}}(\tilde{\mathbf{x}}, \kappa_y, \omega)$ and $\tilde{\mathbf{t}}_{\mathrm{s}}(\tilde{\mathbf{x}}, \kappa_y, \omega)$ in the reference cell $\tilde{\Omega}_{\mathrm{s}}^{\mathrm{e}}$ (figure 1b), where a tilde on a variable denotes its representation in the wavenumber-frequency domain. Only a line of N_x resonators within the reference cell $\tilde{\Omega}_{\mathrm{s}}^{\mathrm{e}}$ is therefore modeled, reducing the summation term in equation (5) to N_x resonators.

In case of structures connected between cells (e.g. periodic track in tunnels), kinematic bases that obey the periodicity condition of the second kind which depend on the wavenumber are employed [14]. The resonators used in the present paper, however, are not connected between cells, and hence, there is no need to adapt the eigenmodes computed from classical FE matrices. These are chosen as the basis in a Craig-Bampton substructuring technique. The periodicity is therefore incorporated in the soil stiffness matrix $\tilde{\mathbf{K}}_{jk}^{\mathrm{s}}(\kappa_y, \omega)$ and the force vector $\underline{\tilde{\mathbf{f}}}_j^{\mathrm{s}}(\kappa_y, \omega)$ using Green-Floquet fundamental solutions $\tilde{\mathbf{u}}^{\mathrm{GF}}(\tilde{\mathbf{x}}', \tilde{\mathbf{x}}, \kappa_y, \omega)$ computed as [10]:

$$\tilde{\mathbf{u}}^{\mathrm{GF}}(\tilde{\mathbf{x}}', \tilde{\mathbf{x}}, \kappa_y, \omega) = \sum_{n_y'=-N_c}^{N_c} \hat{\mathbf{u}}^{\mathrm{G}}(\tilde{\mathbf{x}}' + n_y' L\mathbf{e}_y, \tilde{\mathbf{x}}, \omega)\exp\left(+\mathrm{i}n_y' L\kappa_y\right), \tag{22}$$

where the Green's tensor $\hat{\mathbf{u}}^{\mathrm{G}}(\tilde{\mathbf{x}}' + n_y' L\mathbf{e}_y, \tilde{\mathbf{x}}, \omega)$ represents the displacement fields in the point $\tilde{\mathbf{x}}$ due to sources that are periodically located in space at $\tilde{\mathbf{x}}' + n_y' L\mathbf{e}_y$ and the infinite sum in equation (18) was truncated by a finite sum $n_y' = -N_c$ to N_c.

Using the Green-Floquet fundamental solutions, equation (15) becomes:

$$\boldsymbol{\Phi}_{\mathrm{r}j}^{\mathrm{T}}\left[\mathbf{K}_j - \omega^2\mathbf{M}_j\right]\boldsymbol{\Phi}_{\mathrm{r}j}\underline{\tilde{\boldsymbol{\alpha}}}_{\mathrm{r}j} + \sum_{k=1}^{N_x}\boldsymbol{\Phi}_{\mathrm{r}j}^{\mathrm{T}}\tilde{\mathbf{K}}_{jk}^{\mathrm{s}}\boldsymbol{\Phi}_{\mathrm{r}k}\underline{\tilde{\boldsymbol{\alpha}}}_{\mathrm{r}k} = \boldsymbol{\Phi}_{\mathrm{r}j}^{\mathrm{T}}\underline{\tilde{\mathbf{f}}}_j^{\mathrm{s}}. \tag{23}$$

The tractions $\underline{\tilde{\mathbf{t}}}_{\mathrm{s}k}(\kappa_y, \omega)$ on the interface Σ_k are evaluated within the periodic domain $\tilde{\Omega}_{\mathrm{s}}^{\mathrm{e}}$ using the representation of equation (10) in the wavenumber-frequency domain:

$$\sum_{k=1}^{N_x}\left[\mathbf{I}_{jk} + \tilde{\mathbf{T}}_{jk}\right]\underline{\tilde{\mathbf{u}}}_{\mathrm{s}k} = \sum_{k=1}^{N_x}\tilde{\mathbf{U}}_{jk}\underline{\tilde{\mathbf{t}}}_{\mathrm{s}k}. \tag{24}$$

Equation (24) requires the computation of $\tilde{\mathbf{U}}_{jk}(\kappa_y, \omega)$ and $\tilde{\mathbf{T}}_{jk}(\kappa_y, \omega)$ which are obtained using the Green-Floquet fundamental solutions (22).

The radiated wave field $\underline{\tilde{\mathbf{u}}}_{\mathrm{s}}^{\mathrm{r}}(\tilde{\mathbf{x}}, \kappa_y, \omega)$ in the domain $\tilde{\Omega}_{\mathrm{s}}^{\mathrm{e}}$ is computed using equation (17) in the wavenumber-frequency domain and limiting the number of resonators to N_x. Its spatial-frequency domain representation $\underline{\hat{\mathbf{u}}}_{\mathrm{s}}^{\mathrm{r}}(\mathbf{x}, \omega)$ defined in $\Omega_{\mathrm{s}}^{\mathrm{e}}$ is obtained using the inverse Floquet transform (21).

3 Application: seismic metasurface as a mitigation measure

3.1 Problem outline

A uniform array of resonators interacting with a homogeneous halfspace is considered. The dynamic soil characteristics are summarized in table 1. We investigate the vibration mitigation performance of metasurfaces with six rows of resonators ($N_x = 6$) in the x-direction and $N_y = 7, 21,$ and ∞ resonators in the y-direction. These are denoted as $\mathrm{MS1}$, $\mathrm{MS2}$, and $\mathrm{MS3}$, respectively. Lattice constants $a_x = 1\,\mathrm{m}$ and $a_y = 1.5\,\mathrm{m}$ are considered. A resonator is composed of an oscillator on top of a surface foundation. The oscillator has mass of $50\,\mathrm{kg}$ and resonance frequency of $\mathrm{f_{res}} = 60\,\mathrm{Hz}$. A damping ratio $\xi = 0.01$ is incorporated. The foundation is a rigid concrete slab of dimension $0.5\,\mathrm{m} \times 0.5\,\mathrm{m} \times 0.1\,\mathrm{m}$ and mass $62.5\,\mathrm{kg}$. The metasurface is placed at a distance $D = 12\,\mathrm{m}$ so that mainly Rayleigh waves impinge on the resonators.

Layer	h [m]	C_{s} [m/s]	C_{p} [m/s]	β_{s} [-]	β_{p} [-]	ρ [kg/m^3]
1	∞	150	300	0.020	0.020	1800

Table 1: Dynamic soil characteristics for the homogeneous soil.

3.2 Algorithmic parameters

Calculations are made for frequencies between $40\,\mathrm{Hz}$ and $80\,\mathrm{Hz}$ with a frequency bin of $1\,\mathrm{Hz}$. A logarithmic sampling is adopted for the horizontal wavenumber k_x in both 3D and periodic models, whereas a linear sampling is used for the wavenumber κ_y with $\Delta\kappa_y = 2\pi/(N_c L)$. All computations were performed on 11th Gen Intel® Core™ i7-11850H ($2.50\,\mathrm{GHz}$) CPUs and $32\,\mathrm{Gb}$ RAM.

The homogeneous soil in table 1 has a Rayleigh wavelength $\lambda_{\mathrm{R}} = C_{\mathrm{R}}/f_{\max} = 1.75\,\mathrm{m}$ at $80\,\mathrm{Hz}$. A BE mesh consisting of 6×6 square 4-node linear elements is used, ensuring an accurate BE solution in the chosen frequency range.

The period L influences the required number of terms N_c in the Floquet summation (22) as it changes the distance $N_c L$ between the periodic sources [15]. In addition to this, N_c also depends on the wavelength at a selected frequency, which is affected by the dynamic soil characteristics. Computations are obtained using $N_c = [90, 67]$ for a frequency band split into two ranges as $[(40-60), (61-80)]$ Hz. These correspond to a maximum distance $N_c L = [135, 100.5]\,\mathrm{m}$ from the source within the reference cell $\tilde{\Omega}_{\mathrm{s}}^{\mathrm{e}}$, ensuring that the periodic sources are far enough from the receiver points in the corresponding frequency bands. In cases where metasurfaces are on top of highly damped soils where elastic waves vanish at shorter distances, N_c can be decreased yielding a significant reduction in computational cost.

3.3 Vibration mitigation performance

Figure 2 presents the real part of the vertical displacement $\hat{\mathrm{u}}_{zz}(\mathbf{x}, \mathbf{x}', \omega)$ on a large grid of receiver points on the surface of the homogeneous halfspace at $56\,\mathrm{Hz}$, $57\,\mathrm{Hz}$, and $58\,\mathrm{Hz}$ for $\mathrm{MS1}$, $\mathrm{MS2}$, and $\mathrm{MS3}$. Black lines connect the source location to the closest corners of the metasurface, delimiting the zone affected by the metasurface. A black square depicts a resonator. Black circles display receiver points behind the array of resonators at $x = 31\,\mathrm{m}$ and $y = 0$, $10\,\mathrm{m}$, and $20\,\mathrm{m}$, denoted as $\mathrm{R1}$, $\mathrm{R2}$, and $\mathrm{R3}$. $\mathrm{MS1}$ and $\mathrm{MS2}$ are computed using a 3D FE-BE model [4], while $\mathrm{MS3}$ is evaluated using the periodic FE-BE model.

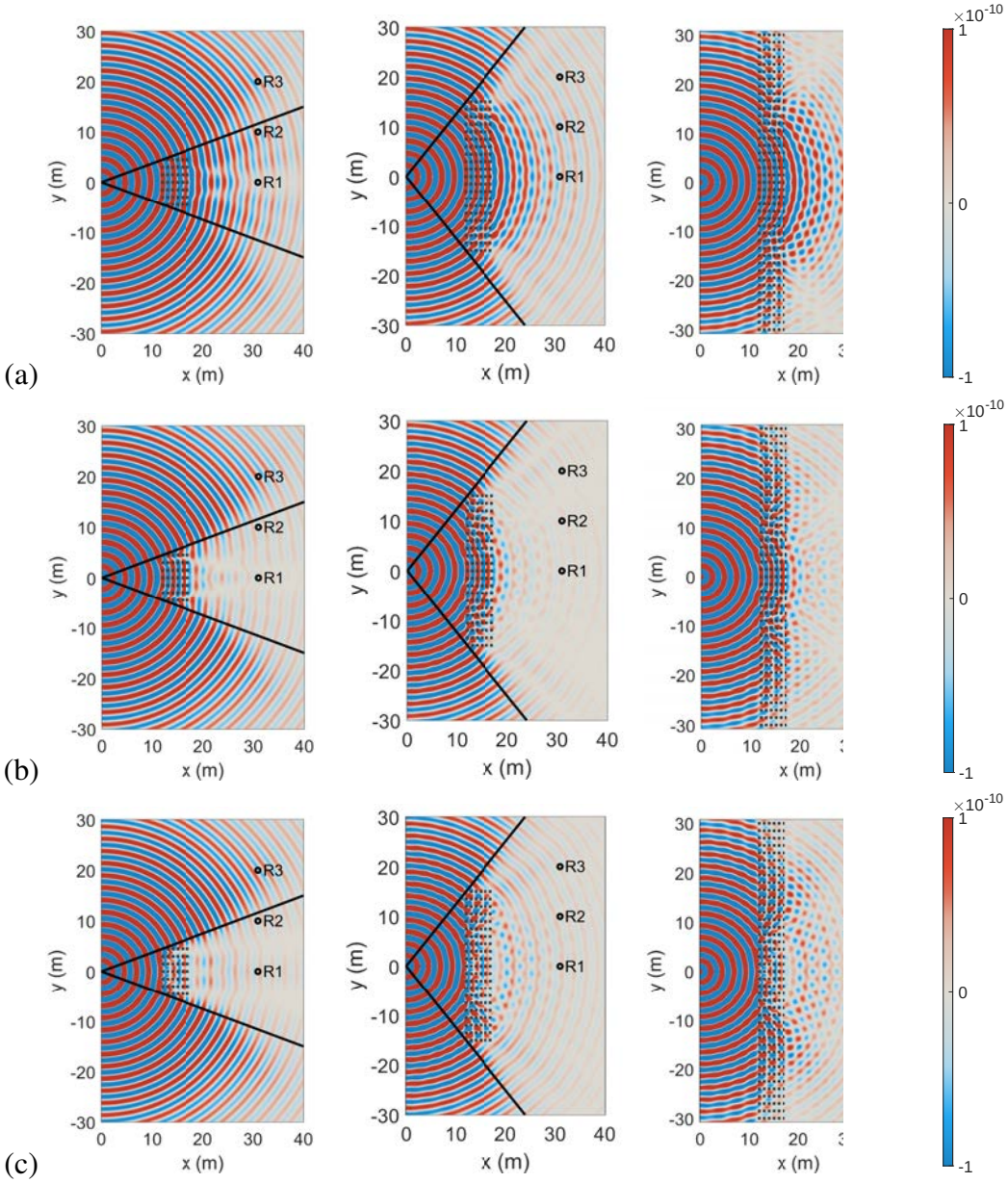

Figure 2: Real part of the vertical displacement $\hat{u}_{zz}(\mathbf{x}, \mathbf{x}', \omega)\,[\mathrm{m/Hz}]$ at (a) $56\,\mathrm{Hz}$, (b) $57\,\mathrm{Hz}$, and (c) $58\,\mathrm{Hz}$ on the surface ($z = 0$) of the homogeneous soil for $\mathrm{MS1}$ (left), $\mathrm{MS2}$ (middle), and $\mathrm{MS3}$ (right). Black lines connect the source to the corners of the metasurface.

Significant vibration reduction is found behind the metasurfaces within the shielded zone.

At $56\,\mathrm{Hz}$ (figure 2a), this is less pronounced as this frequency is relatively far from the resonance frequency of the resonators. The Rayleigh wave at $57\,\mathrm{Hz}$ and $58\,\mathrm{Hz}$ (figure 2b and 2c) interacting with the resonators splits into three portions, which propagate in the x-, $-y$-, and $+y$-direction. The waves traveling in the y-direction are not significantly affected by $\mathrm{MS1}$ as only three rows of resonators are not enough to attenuate the wave field. As a result, vibration is amplified outside the shielded zone, near its borders. This is no longer the case for $\mathrm{MS2}$ and $\mathrm{MS3}$ as the Rayleigh waves propagating in the y-direction are attenuated by the large number of resonators in this direction. A more important scattered wave field behind $\mathrm{MS2}$ and $\mathrm{MS3}$ in comparison to $\mathrm{MS1}$ is observed at these frequencies.

Figure 3 shows the insertion loss $\widehat{\mathrm{IL}}(\mathbf{x},\omega)$ of the vertical displacement at $\mathrm{R1}$, $\mathrm{R2}$, and $\mathrm{R3}$ on a logarithmic scale in dB for metasurfaces considered in figure 2. The insertion loss is defined as the ratio of the vertical displacement amplitude without and with the metasurface. Positive values of the insertion loss indicate a reduction of the vertical free field vibrations. A sharp peak in the insertion loss at the resonance frequency of the system is observed indicating significant vibration attenuation.

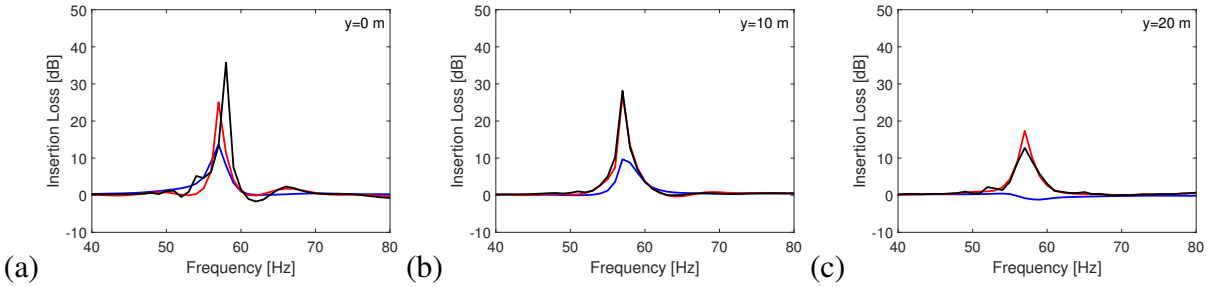

Figure 3: Insertion loss $\widehat{\mathrm{IL}}(x = 31\,\mathrm{m}, y, z = 0, \omega)$ on the surface of the soil at (a) $\mathrm{R1}$, (b) $\mathrm{R2}$, and (c) $\mathrm{R3}$, for $\mathrm{MS1}$ (blue), $\mathrm{MS2}$ (red), and $\mathrm{MS3}$ (black).

Although all configurations generate vibration reduction at $\mathrm{R1}$ at $56\,\mathrm{Hz}$, $57\,\mathrm{Hz}$, and $58\,\mathrm{Hz}$ (figure 2), figure 3a reveals a significant impact on the metasurface's efficiency of the number of resonators in the longitudinal direction. The frequency where the peak is observed and the vibration attenuation performance is influenced by N_y, where a change in this term results in an alteration in the mass density of the system, leading to a shift in frequency. For $\mathrm{MS1}$ and $\mathrm{MS2}$, a peak at $57\,\mathrm{Hz}$ is found. Infinitely extending the metasurface in the y-direction induces a shift of the peak to $58\,\mathrm{Hz}$, as well as boosts the vibration mitigation performance, as larger peak values are found for $\mathrm{MS3}$.

Peaks at the same frequency for the different metasurfaces are found when the insertion loss is evaluated at $\mathrm{R2}$ (figure 3b). A good agreement between the insertion loss of $\mathrm{MS2}$ and $\mathrm{MS3}$ is observed. The vibration mitigation performance of the metasurfaces is reduced at $\mathrm{R2}$ in comparison to the performance seen at $\mathrm{R1}$ (figure 3a).

Figure 3c shows the insertion loss at $\mathrm{R3}$. This receiver is outside the zone protected by $\mathrm{MS1}$ as depicted in figure 2, resulting in $\widehat{\mathrm{IL}} \approx 0$. Slightly negative values of insertion loss are obtained around the resonance frequency of the system due to the vibration amplification near the borders of the shielded zone. The peak values for $\mathrm{MS2}$ and $\mathrm{MS3}$ are distinguishable. More energy travels in the direction of $\mathrm{R3}$ behind $\mathrm{MS3}$ (figure 2b), resulting in a lower value of insertion loss at $57\,\mathrm{Hz}$ at this location in comparison to the response for $\mathrm{MS2}$.

The peak values of the insertion loss for all metasurfaces are reduced at farther points, indicating that the performance decreases with distance.

Similar results are obtained with the periodic model when the (finite) metasurface is effectively long in the y-direction. This indicates that the periodic method can be used as an alternative for a 3D model when the metasurface is long enough in the y-direction. Further investigation should be done to precisely quantify how long the metasurface has to be.

3.4 Computational performance

Table 2 summarizes the number of degrees of freedom N_{DOF}, required memory to compute the boundary element matrices $\hat{\mathbf{U}}(\omega)$ and $\tilde{\mathbf{U}}(\kappa_y, \omega)$, the transfer matrices $\hat{\mathbf{U}}_{\mathrm{p}}(\mathbf{x}, \omega)$ and $\tilde{\mathbf{U}}_{\mathrm{p}}(\tilde{\mathbf{x}}, \kappa_y, \omega)$, and the CPU time to compute the response for all metasurfaces considered in figures 2 (case 1) and 3 at a single frequency (case 2). These matrices contain complex floating point entries in double precision.

	N_y [$-$]	N_{DOF} [$-$]	$\hat{\mathbf{U}}$ [Gb]	$\hat{\mathbf{U}}_{\mathrm{p}}$ [Gb]	Time (case 1) [s]	Time (case 2) [s]
MS1	7	6 174	0.57	16.70	1 368	118.8
MS2	21	18 522	1.96	50.10	7 920	1 620
	N_c [$-$]	N_{DOF} [$-$]	$\tilde{\mathbf{U}}$ [Gb]	$\tilde{\mathbf{U}}_{\mathrm{p}}$ [Gb]	Time (case 1) [s]	Time (case 2) [s]
MS3	67	882	0.01	0.55	55 074	8710
MS3	90	882	0.01	0.55	97 897	15 702

Table 2: Required memory to compute the boundary element matrices $\hat{\mathbf{U}}(\omega)$ and $\tilde{\mathbf{U}}(\kappa_y, \omega)$, the transfer matrices $\hat{\mathbf{U}}_{\mathrm{p}}(\mathbf{x}, \omega)$ and $\tilde{\mathbf{U}}_{\mathrm{p}}(\tilde{\mathbf{x}}, \kappa_y, \omega)$, and the CPU time to compute the response at a single frequency in figures 2 (case 1) and 3 (case 2).

In a 3D BE computation, a quadratic amount of memory ($\mathcal{O}(N_{\mathrm{DOF}}^2)$) in terms of the number of degrees of freedom N_{DOF} of the BE mesh is required to store $\hat{\mathbf{U}}(\omega)$. In order to solve equation (10) by means of direct solvers, for instance an LU-decomposition, a cubic amount of operations is demanded ($\mathcal{O}(N_{\mathrm{DOF}}^3)$). Therefore, using a 3D FE-BE model to assess the performance of a very long and wide metabarrier is limited by excessive memory requirements.

An amount of memory of $\mathcal{O}(N_{\mathrm{DOF_s}} N_{\mathrm{DOF}})$ is required to store the transfer matrix $\hat{\mathbf{U}}_{\mathrm{p}}(\mathbf{x}, \omega)$, where $N_{\mathrm{DOF_s}}$ is the number of degrees of freedom at all receiver points. MS2 requires $50.1\,\mathrm{Gb}$ to store this matrix, exceeding the RAM limits of the machine. Nevertheless, as the response at receiver points can be calculated separately, the wave field on a large grid can still be obtained. Storing this matrix for reuse to compute different superstructures requires a high amount of disk storage preventing parametric studies using this formulation.

A quadratic amount of memory is still required to store the boundary element matrix $\tilde{\mathbf{U}}(\kappa_y, \omega)$ in a periodic FE-BE model. However, the number of degrees of freedom N_{DOF} in the BE mesh is drastically reduced as modeling of only a line of resonators is needed. This model can therefore be used to compute the solution of metasurfaces with large number of resonators N_x.

The amount of memory necessary to store the transfer matrix $\tilde{\mathbf{U}}_{\mathrm{p}}(\tilde{\mathbf{x}}, \kappa_y, \omega)$ is also significantly lowered in comparison to a 3D BE computation. As the free field is restrained to the reference cell $\tilde{\Omega}_{\mathrm{s}}^{\mathrm{e}}$, $N_{\mathrm{DOF_s}}$ also reduces. This reduces the disk space required to store this matrix, enabling saving and reusing this matrix for further computations where only the superstructure is modified.

Besides using Green-Floquet fundamental solutions (22), the periodic FE-BE model requires a BE computation for all wavenumbers. As a result, the 3D FE-BE method turn out to be faster

than the periodic FE-BE model for moderate problem sizes. Periodic models can be an attractive alternative in cases where longer finite metasurfaces are needed (e.g. railway induced vibration). Moreover, since a significant decrease in CPU time is experienced when N_c is reduced (table 2), larger a_y or highly damped soils result in higher efficiency of the periodic FE-BE model as convergence can be achieved for smaller values of N_c.

4 Conclusions

The effect of the length of 2D seismic metasurfaces on vibration mitigation performance has been investigated. This is accomplished using 3D and periodic FE-BE models. Results for three metasurfaces with increasing N_y approaching the have been presented. Behind longer metasurfaces, larger vibration reduction is found in a perpendicular direction from the source. Similar results are obtained in diagonal directions when the finite metasurface is effectively long in the y-direction. Finally, the vibration mitigation performance of the metasurfaces reduces with distance in the y-direction.

The computational efficiency of the periodic model has been compared with the 3D FE-BE approach. Although using a periodic FE-BE model results in a significant reduction in memory requirements, the CPU time to solve the problem increases in comparison to the 3D FE-BE model. This, however, strongly depends on the required number of terms N_c in the Floquet transformation, which depends on the period L and the soil properties. For a large period L and highly damped soils, the periodic FE-BE model can be more efficient than the 3D model as N_c is significantly reduced.

Acknowledgement

Results presented in this paper were obtained within the frame of the project G0B8221N "Mitigation of railway induced vibration using seismic metamaterials" funded by the Research Foundation Flanders (FWO Flanders). The financial support is gratefully acknowledged.

REFERENCES

[1] D. Colquitt, A. Colombi, R. Craster, P. Roux, and S. Guenneau, "Seismic metasurfaces: Sub-wavelength resonators and rayleigh wave interaction," *Journal of the Mechanics and Physics of Solids*, vol. 99, pp. 379–393, 2017.

[2] A. Palermo, S. Krödel, A. Marzani, and C. Daraio, "Engineered metabarrier as shield from seismic surface waves," *Scientific reports*, vol. 6, no. 1, pp. 1–10, 2016.

[3] C. He, S. Zhou, X. Li, H. Di, and X. Zhang, "Forest trees as a natural metamaterial for surface wave attenuation in stratified soils," *Construction and Building Materials*, vol. 363, p. 129769, 2023.

[4] D. Carneiro, H. Kato, P. Reumers, G. Lombaert, and G. Degrande, "Mitigation of environmental ground vibration using seismic metasurfaces," in *Proceedings of the 30th International Conference on Noise and Vibration Engineering, ISMA 2022* (W. Desmet, B. Pluymers, D. Moens, and S. Neeckx, eds.), (Leuven, Belgium), pp. 3247–3261, September 2022.

[5] S. Brûlé, E. Javelaud, S. Enoch, and S. Guenneau, "Experiments on seismic metamaterials: molding surface waves," *Physical review letters*, vol. 112, no. 13, p. 133901, 2014.

[6] A. Colombi, P. Roux, S. Guenneau, P. Gueguen, and R. V. Craster, "Forests as a natural seismic metamaterial: Rayleigh wave bandgaps induced by local resonances," *Scientific reports*, vol. 6, no. 1, pp. 1–7, 2016.

[7] A. Colombi, D. Colquitt, P. Roux, S. Guenneau, and R. Craster, "A seismic metamaterial: The resonant metawedge," *Scientific reports*, vol. 6, no. 1, pp. 1–6, 2016.

[8] A. Palermo, M. Vitali, and A. Marzani, "Metabarriers with multi-mass locally resonating units for broad band rayleigh waves attenuation," *Soil Dynamics and Earthquake Engineering*, vol. 113, pp. 265–277, 2018.

[9] C. Zeng, C. Zhao, and F. Zeighami, "Seismic surface wave attenuation by resonant metasurfaces on stratified soil," *Earthquake Engineering & Structural Dynamics*, vol. 51, no. 5, pp. 1201–1223, 2022.

[10] D. Clouteau, M. Elhabre, and D. Aubry, "Periodic BEM and FEM-BEM coupling: application to seismic behaviour of very long structures," *Computational Mechanics*, vol. 25, pp. 567–577, 2000.

[11] D. Aubry and D. Clouteau, "A subdomain approach to dynamic soil-structure interaction," in *Recent advances in Earthquake Engineering and Structural Dynamics* (V. Davidovici and R. Clough, eds.), pp. 251–272, Nantes: Ouest Editions/AFPS, 1992.

[12] S. François, *Nonlinear modelling of the response of structures due to ground vibrations*. PhD thesis, Department of Civil Engineering, KU Leuven, 2008.

[13] R. R. Craig Jr and M. C. Bampton, "Coupling of substructures for dynamic analyses.," *AIAA journal*, vol. 6, no. 7, 1968.

[14] G. Degrande, D. Clouteau, R. Othman, M. Arnst, H. Chebli, R. Klein, P. Chatterjee, and B. Janssens, "A numerical model for ground-borne vibrations from underground railway traffic based on a periodic finite element - boundary element formulation," *Journal of Sound and Vibration*, vol. 293, no. 3-5, pp. 645–666, 2006.

[15] S. Gupta, M. Hussein, G. Degrande, H. Hunt, and D. Clouteau, "A comparison of two numerical models for the prediction of vibrations from underground railway traffic," *Soil Dynamics and Earthquake Engineering*, vol. 27, no. 7, pp. 608–624, 2007.